

**REPORT DOCUMENTATION PAGE**

Form Approved  
OMB No. 0704-0188

The public reporting burden for this collection of information is estimated to average 1 hour per response, including the time for reviewing instructions, searching existing data sources, gathering and maintaining the data needed, and completing and reviewing the collection of information. Send comments regarding this burden estimate or any other aspect of this collection of information, including suggestions for reducing the burden, to the Department of Defense, Executive Services and Communications Directorate (0704-0188). Respondents should be aware that notwithstanding any other provision of law, no person shall be subject to any penalty for failing to comply with a collection of information if it does not display a currently valid OMB control number.

PLEASE DO NOT RETURN YOUR FORM TO THE ABOVE ORGANIZATION.

1. REPORT DATE (DD-MM-YYYY) 04-08-2005		2. REPORT TYPE Journal Article (refereed)		3. DATES COVERED (From - To)	
4. TITLE AND SUBTITLE Yellow Sea ocean-acoustic solitary wave modeling studies				5a. CONTRACT NUMBER	
				5b. GRANT NUMBER	
				5c. PROGRAM ELEMENT NUMBER 62435N	
6. AUTHOR(S) *Warn-Varnas, A.C., *Ching-Bing, S. A., *King, D.B., Hawkins, J.A., Lamb, K. G., Teixeira, M.				5d. PROJECT NUMBER	
				5e. TASK NUMBER	
				5f. WORK UNIT NUMBER 73-6621-B5	
7. PERFORMING ORGANIZATION NAME(S) AND ADDRESS(ES) Naval Research Laboratory Oceanography Division Stennis Space Center, MS 39529-5004				8. PERFORMING ORGANIZATION REPORT NUMBER NRL/JA/7320-02-0010	
9. SPONSORING/MONITORING AGENCY NAME(S) AND ADDRESS(ES) Office of Naval Research 800 N. Quincy St. Arlington, VA 22217-5660				10. SPONSOR/MONITOR'S ACRONYM(S) ONR	
				11. SPONSOR/MONITOR'S REPORT NUMBER(S)	
12. DISTRIBUTION/AVAILABILITY STATEMENT Approved for public release, distribution is unlimited.					
13. SUPPLEMENTARY NOTES <i>U.S. Govt authors: Warn-Varnas; Ching-Bing, King</i>					
14. ABSTRACT This study is in an area south of the Shandong peninsula, near the region where Zhou et al. (1991) observed anomalous drops in acoustical intensity. Solitary wave generation and propagation simulations are performed using the Lamb (1994) nonhydrostatic model. The model simulations show that, for summer conditions, the existing semi-diurnal tidal flow over the topographic variations formed internal bores and solitary waves. For the Shandong area, we analyzed summer observations from Synthetic Aperture Radar (SAR) that tracked solitary wave trains from their surface roughness signatures. The images contained seven events consisting of internal bores and solitary waves that traveled in a well-defined direction for 2.5 days. The origin of the trains appeared at a well-defined point along a steep topographic drop. The SAR observations guided and tuned the model simulations, by comparing spectra of observed and modeled wavelengths. The tuned model yields wavelengths within factors of 2, or less, of those derived from SAR data. Wavelength and amplitude dispersion analysis showed two dispersion regimes. Modeled phase speeds were at the lower limit of phase speeds deduced from SAR data, from about 0.8 to 1.0 m/s. Acoustical intensity calculations in the presence of solitary wave trains will be undertaken in a subsequent paper using a parabolic equation acoustical model along the path of solitary wave train propagation.					
15. SUBJECT TERMS Shandong peninsula, Synthetic Aperture Radar (SAR), solitary wave trains, wavelength dispersion					
16. SECURITY CLASSIFICATION OF:			17. LIMITATION OF ABSTRACT UL	18. NUMBER OF PAGES 15	19a. NAME OF RESPONSIBLE PERSON A. C. Warn-Varnas
a. REPORT Unclassified	b. ABSTRACT Unclassified	c. THIS PAGE Unclassified			19b. TELEPHONE NUMBER (Include area code) 228-688-5223

**PUBLICATION OR PRESENTATION RELEASE REQUEST**

Pubkey: 3405

NRLINST 5600.2

1. REFERENCES AND ENCLOSURES	2. TYPE OF PUBLICATION OR PRESENTATION	3. ADMINISTRATIVE INFORMATION
Ref: (a) NRL Instruction 5600.2 (b) NRL Instruction 5510.40D  Encl: (1) Two copies of subject paper (or abstract)	<input type="checkbox"/> Abstract only, published <input type="checkbox"/> Book <input type="checkbox"/> Conference Proceedings (refereed) <input type="checkbox"/> Invited speaker <input checked="" type="checkbox"/> Journal article (refereed) <input type="checkbox"/> Oral Presentation, published <input type="checkbox"/> Other, explain	<input type="checkbox"/> Abstract only, not published <input type="checkbox"/> Book chapter <input type="checkbox"/> Conference Proceedings (not refereed) <input type="checkbox"/> Multimedia report <input type="checkbox"/> Journal article (not refereed) <input type="checkbox"/> Oral Presentation, not published
		STRN <u>NRL/JA/7320-02-10</u> Route Sheet No. <u>7320/</u> Job Order No. _____ Classification <input checked="" type="checkbox"/> U <input type="checkbox"/> C Sponsor _____ approval obtained <input checked="" type="checkbox"/> yes <input type="checkbox"/> no

**4. AUTHOR**

Title of Paper or Presentation  
**Yellow Sea Ocean-Acoustic Solitary Wave Modelling Studies**

Author(s) Name(s) (First, MI, Last), Code, Affiliation if not NRL  
**Alex C. WarnVarnas, S. Chin-Bing, D. King, J. D. Hawkins, K Lamb, Marvi Teixeira**

It is intended to offer this paper to the \_\_\_\_\_  
 (Name of Conference)

\_\_\_\_\_  
 (Date, Place and Classification of Conference)

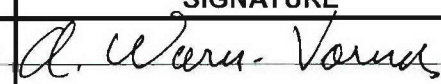
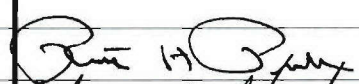
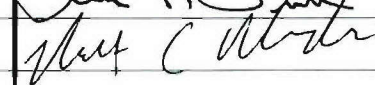

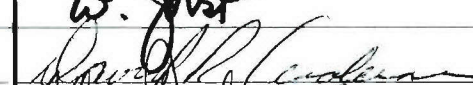
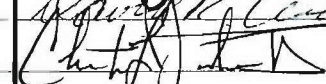
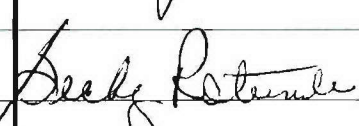
and/or for publication in Journal of Geophysical Research, Unclassified  
 (Name and Classification of Publication) (Name of Publisher)

After presentation or publication, pertinent publication/presentation data will be entered in the publications data base, in accordance with reference (a).

It is the opinion of the author that the subject paper (is \_\_\_\_\_) (is not ) classified, in accordance with reference (b).  
 This paper does not violate any disclosure of trade secrets or suggestions of outside individuals or concerns which have been communicated to the Laboratory in confidence. This paper (does \_\_\_\_\_) (does not ) contain any militarily critical technology.  
 This subject paper (has \_\_\_\_\_) (has never ) been incorporated in an official NRL Report.

**Alex C. WarnVarnas, 7322**  
 Name and Code (Principal Author)  (Signature)

**5. ROUTING/APPROVAL**

CODE	SIGNATURE	DATE	COMMENTS
Author(s) Warn-Varnas		9/30/02	
Section Head Preller		10/2/02	
Branch Head Rhodes (acting)		10/2/02	
Division Head William J. Jobst, 7300		10/4	1. Release of this paper is approved. 2. To the best knowledge of this Division, the subject matter of this paper (has _____) (has never <input checked="" type="checkbox"/> ) been classified.
Security, Code 7030.1		10/8	1. Paper or abstract was released. 2. A copy is filed in this office. <i>SSC-438-02</i>
Office of Counsel, Code 1008.3		10/15	
ADOR/Director NCST E.O. Hartwig, 7000			
Public Affairs (Unclassified/ Unlimited Only), Code 7030.4		10/8/02	Please add acknowledgments w/PE#
Division, Code			
Author, Code			

## Yellow Sea ocean-acoustic solitary wave modeling studies

A. C. Warn-Varnas,<sup>1</sup> S. A. Chin-Bing,<sup>1</sup> D. B. King,<sup>1</sup> J. A. Hawkins,<sup>2</sup> K. G. Lamb,<sup>3</sup>  
and M. Teixeira<sup>4</sup>

Received 10 November 2004; revised 21 January 2005; accepted 17 March 2005; published 4 August 2005.

[1] This study is in an area south of the Shandong peninsula, near the region where Zhou et al. (1991) observed anomalous drops in acoustical intensity. Solitary wave generation and propagation simulations are performed using the Lamb (1994) nonhydrostatic model. The model simulations show that, for summer conditions, the existing semi-diurnal tidal flow over the topographic variations formed internal bores and solitary waves. For the Shandong area, we analyzed summer observations from Synthetic Aperture Radar (SAR) that tracked solitary wave trains from their surface roughness signatures. The images contained seven events consisting of internal bores and solitary waves that traveled in a well-defined direction for 2.5 days. The origin of the trains appeared at a well-defined point along a steep topographic drop. The SAR observations guided and tuned the model simulations, by comparing spectra of observed and modeled wavelengths. The tuned model yields wavelengths within factors of 2, or less, of those derived from SAR data. Wavelength and amplitude dispersion analysis showed two dispersion regimes. Modeled phase speeds were at the lower limit of phase speeds deduced from SAR data, from about 0.8 to 1.0 m/s. Acoustical intensity calculations in the presence of solitary wave trains will be undertaken in a subsequent paper using a parabolic equation acoustical model along the path of solitary wave train propagation.

**Citation:** Warn-Varnas, A. C., S. A. Chin-Bing, D. B. King, J. A. Hawkins, K. G. Lamb, and M. Teixeira (2005), Yellow Sea ocean-acoustic solitary wave modeling studies, *J. Geophys. Res.*, 110, C08001, doi:10.1029/2004JC002801.

### 1. Introduction

[2] Recent interest in the oceanography of a region of the Yellow Sea south of the Shandong Peninsula can be attributed to the acoustical measurements of shallow-water sound propagation published by Zhou et al. [1991]. They made acoustical measurements in this region over a period of years. Some of their measurements showed an anomalous drop in acoustical intensity of about 15–20 dB at a range of 28 km from the acoustic source. These anomalous losses occurred over a narrow band of acoustic frequencies. For the case they published, the loss was centered around 630 Hz. The anomalous losses were both seasonally and directionally dependent, occurring only in the summer and along tracks perpendicular to the shore. The authors postulated the existence of solitary waves in the thermocline, and attributed the anomalous losses to the interactions of the acoustic signal with the solitary internal waves. The lack of oceanographic data required them to use a model to simulate the solitary wave environment; a gated sine function was used to represent the solitons. A parabolic equation acoustic propagation model was used to perform the transmission loss calculations.

The simulation results from this hypothetical environment showed that an anomalous transmission loss could occur near the same frequency (630 Hz) as evident in the acoustic measurements. Computer simulations by other investigators [Chin-Bing et al., 1993; King et al., 1994] subsequently confirmed that a “resonant-like” transmission loss is caused by an acoustical mode coupling in the presence of solitary waves, together with a corresponding larger bottom attenuation for the coupled acoustic modes. However, the lack of supporting oceanographic information left some doubt as to the soliton hypothesis. Schooling fish [Weston, 1992] were suggested as a possible source of the anomalous loss seen in the data.

[3] In the acoustic calculations the existence of solitary waves has so far been only postulated for the area south of the Shandong Peninsula. This paper addresses this issue by considering solitary wave generation and propagation in the region.

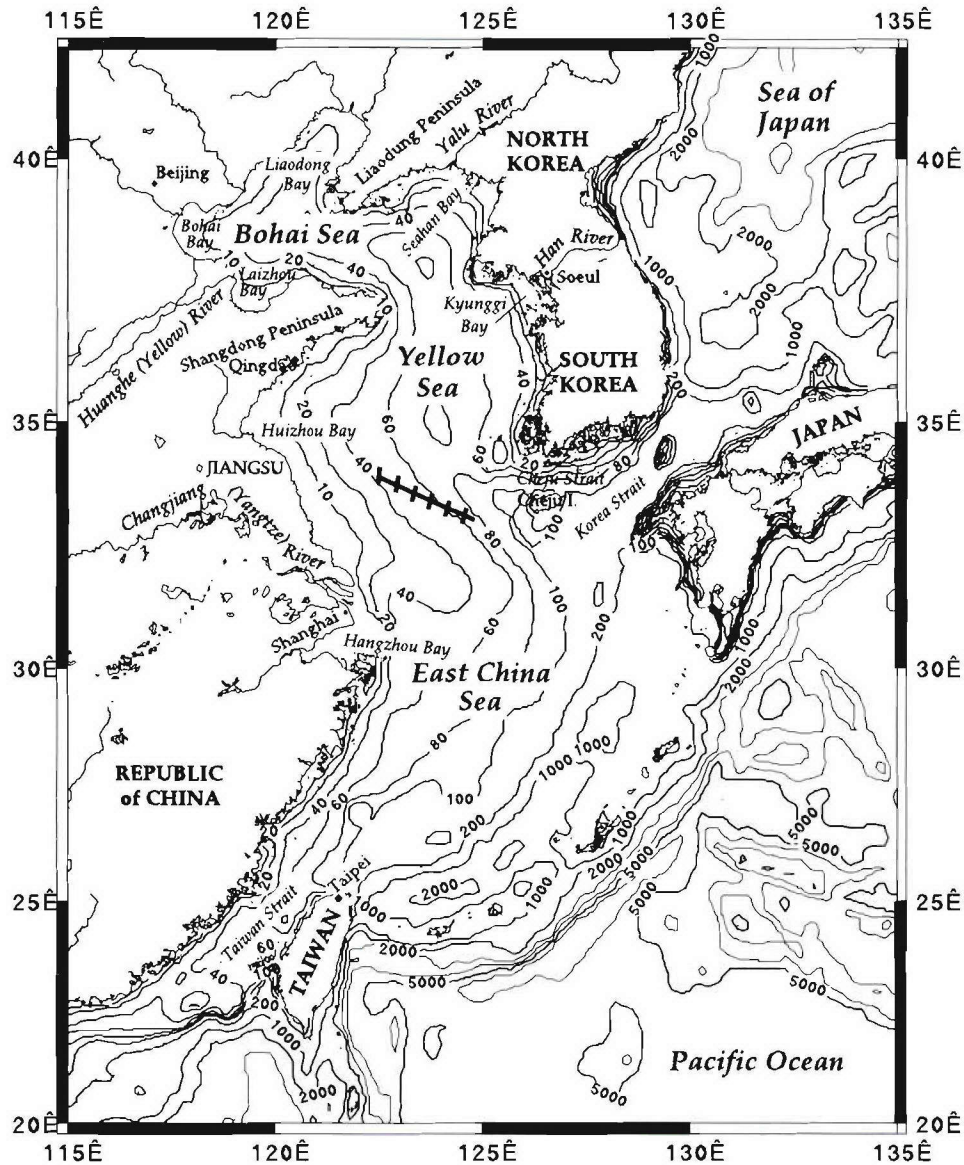
[4] The generation and propagation of solitary waves have been modeled with nonhydrostatic models. Nonhydrostatic modeling of tidal flow over steep topography shows that tidal flow depresses the pycnocline and generates a depression [Lamb, 1994; Brandt et al., 1997; Warn-Varnas et al., 2003]. From the depression, two internal bores are formed propagating in opposite directions. The offshore internal bores propagate and steepen on the leading edge through nonlinear effects. Then frequency and amplitude dispersion sets in and the leading edge disintegrates into solitary waves [Lamb, 1994; Brandt et al., 1997; Warn-

<sup>1</sup>Naval Research Laboratory, Stennis Space Center, Mississippi, USA.

<sup>2</sup>Planning Systems Inc., Slidell, Louisiana, USA.

<sup>3</sup>University of Waterloo, Waterloo, Ontario, Canada.

<sup>4</sup>Polytechnic University of Puerto Rico, Hato Rey, Puerto Rico.



**Figure 1a.** Track of the RADARSAT-1 measurements, black line, located south of the Shandong peninsula. The smaller black lines reflect the orientation of the internal bores and solitary wave trains relative to the direction of propagation.

Varnas *et al.*, 2003]. The onshore propagating internal bore develops a hydraulic jump during semidiurnal tidal reversal, when the flow becomes supercritical [Lamb, 1994; Brandt *et al.*, 1997; Warn-Varnas *et al.*, 2003].

[5] The paper is organized into the following sections. In section 2 the Shandong region and SAR observations of solitary waves are described. In section 3 the numerical simulations of the generation and propagation of solitary wave trains are presented with a discussion of the results. We finish with conclusions in section 4. Simulations of the acoustical field structure and intensity will be published in a separate paper.

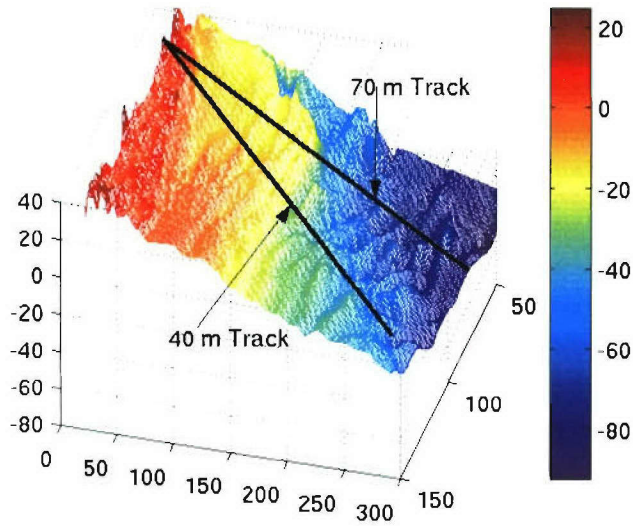
## 2. Shandong Region

### 2.1. Topography of the Region

[6] The Yellow Sea is a shallow sea bounded by China, Korea, and the East China Sea with a maximum depth of

around 80 m in the center. The topography varies gently from the Chinese continent and more rapidly from the Korean peninsula. The present study is located south of the Shandong peninsula and will be referred to as the Shandong area, Figure 1a. The black line shows the track of a solitary wave train observed with RADARSAT-1 Synthetic Aperture Radar (SAR). At the beginning of the arrow, there is a relatively steeper slope, where the first internal bore is observed. The lines across the arrow indicate the along crest direction of the wave packets. The variable angle of the lines suggests refraction along the shelf break.

[7] The topography of the area is extracted from the Digital Atlas of Choi [1999]. This is a bathymetric database for the Yellow Sea and neighboring Sea of the Korean Peninsula. Its construction encompassed all available bathymetry charts. A detailed view of the three-dimensional topography in the area where the satellite transects are located is shown in Figure 1b. A mountainous type of



**Figure 1b.** Three-dimensional topographic distribution according to the digital atlas of *Choi* [1999]. The solid black lines represent 40-m and 70-m tracks from the shelf to deeper areas. The 70-m track is the same as in Figure 1a. Vertical scale is the location relative to the shelf depth in meters. Horizontal scales are in kilometers.

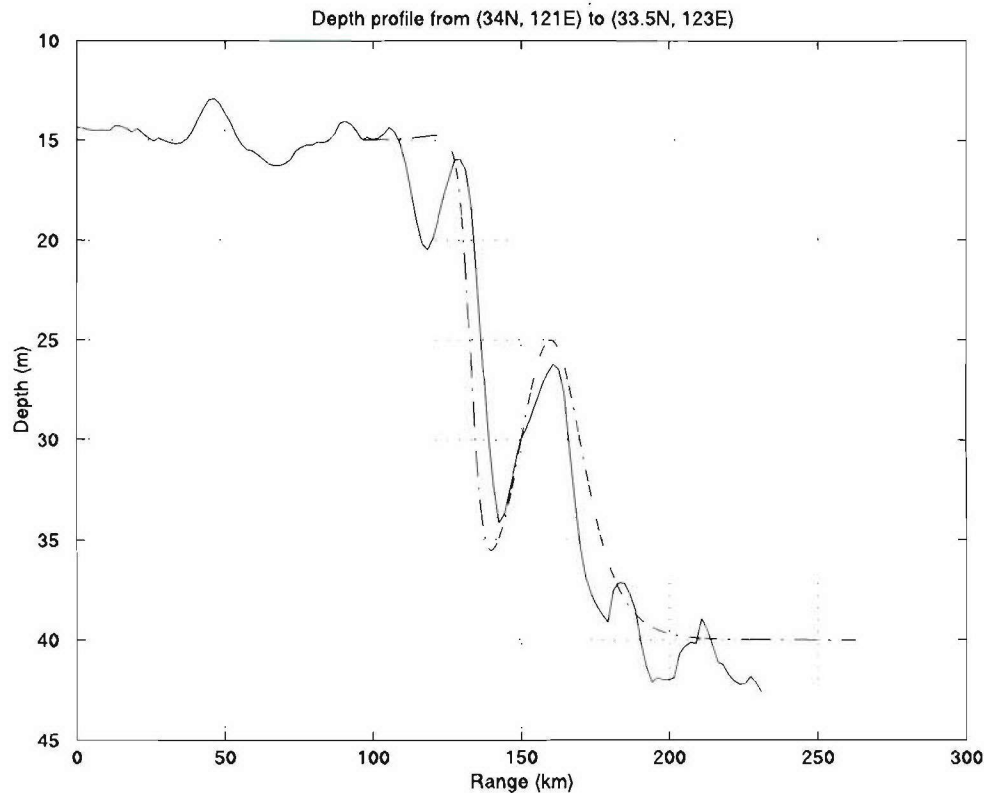
distribution is evident. Along both of the transects, there is a drop nearshore, followed by a rise and a second drop. The maximum depth of the drops depends on which transect is used. The two transects used, indicated in Figure 1, have

final depths of about 40 and 70 m. In Figure 2 the topography along one transect, along with the model representations, is shown. The topography is represented as a combination of hyperbolic functions (shown as the dashed line in Figure 2) because a continuous representation of the bottom is more convenient for the simulations.

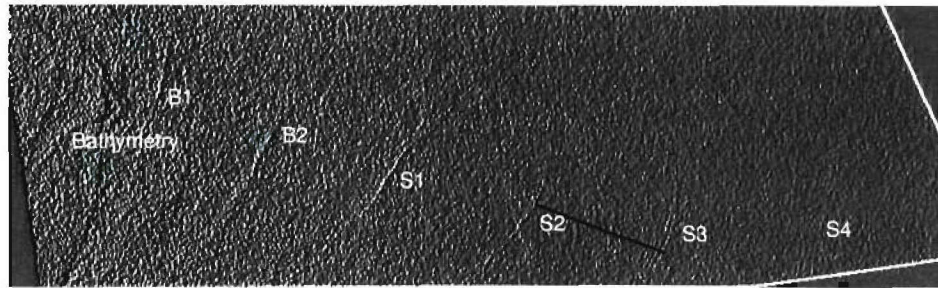
**2.2. SAR Data**

[8] Synthetic Aperture Radar detects the variations in sea surface roughness caused by internal wave currents. The convergence and divergence of the internal wave currents causes surface roughness variations that translates into bright and dark patterns of pixel intensity in the SAR images.

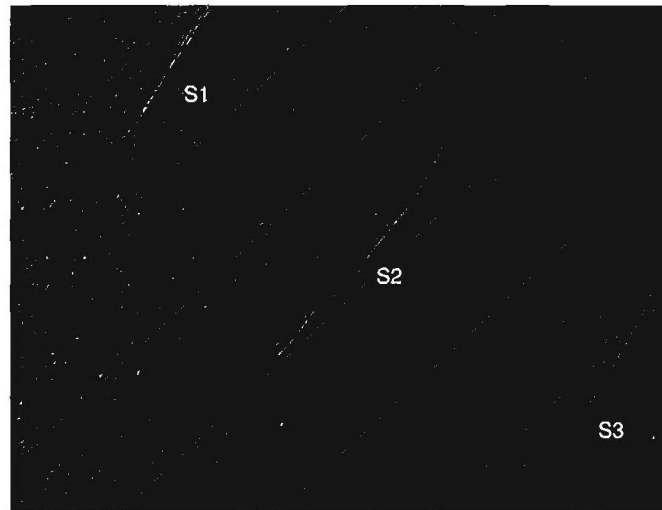
[9] Summer SAR observations were obtained, for the Shandong area, from RADARSAT1 SAR with a 500 by 500 km width observation area. The observations were acquired on 8 August 1998 and processed at the Alaska SAR Facility. The pixel spacing is 100 m. Figure 1a shows the track location of the observations, with the topographic features in the background. In the SAR image, features corresponding to bathymetric variations and to large-amplitude internal waves can be seen (Figures 3a and 3b). The bright curve marked “bathymetry” in Figure 3 corresponds to topographic contours along the shoreline. *Hsu et al.* [2001] has noted the possibility of “seeing” shallow topographic features using SAR images owing to horizontal tidal flow convergence over rapidly changing topography. The features marked B1 and B2 are curved bright lines, which, in light of the model simulations to be presented, possibly correspond to internal hydraulic jumps. There is a possibil-



**Figure 2.** Solid line extracted topography from the digital atlas of *Choi* [1999] along the 40-m track. Dash-dotted line is the approximated topography with an analytical function.



(a.)



(b.)

**Figure 3.** (a) Location of features in RADARSAT1 observations on 8 August 1998. B1 and B2 are internal bores. S1 through S4 indicate a propagating solitary wave train. A bathymetric feature is also present. The solid black line represents a scale of 46 km. (b) Zoom of internal wave solitary wave train at S1, S2, and S3. The solid black line represents a scale of 10 km.

ity that a better pixel resolution might show that the jumps are accompanied by a few waves. The bright curved features marked S1 through S4 are solitary wave trains.

[10] The solitary wave train propagates from about  $34^{\circ}\text{N}$ ,  $122^{\circ}\text{E}$  to  $33.4^{\circ}\text{N}$ ,  $124.5^{\circ}\text{E}$ . A zoom of the first three resolved solitary wave trains is shown in Figure 3b (denoted S1, S2, and S3). The spacing between the bright convergence lines increases as one proceeds from S1 to S3 (also through S4, although this is difficult to see from Figure 3a). This suggests generation in the coastal shelfbreak area. The bright and dark bands mark the surface convergence/divergence caused by the current fields associated with the waves. The spacing between the wave packets has a high degree of regularity along a well-defined direction. The overall concave shape of the wave front is preserved along the travel path, which again suggests that these internal wave packets originated from the same shelf break location.

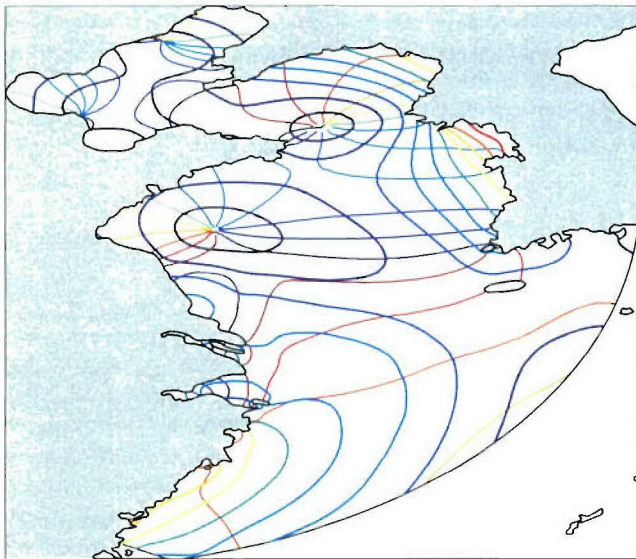
[11] As the solitary wave train travels away from the point of origin, the spacing between solitary waves in the train increases. The distance between the first and the sixth wave packet is about 271 km. Assuming a 12.4-hour semidiurnal

tidal period, the phase speed estimates range from 0.8 to 1.1 m/s along the track.

### 2.3. Tides

[12] The dominant barotropic tidal component in the Yellow Sea is the semidiurnal  $M_2$  tide. Pronounced tidal variations exist along the Chinese and Korean coasts, where the surface elevation changes can be as high as 2 to 2.5 m (Figure 4) [Naimie *et al.*, 2001]. There are strong flood/ebb tidal flow points around the Yangtze River on the Chinese coast and the Han River on the Korean coast (Figure 1a). At these points the tidal flow can radiate out or come into the region [Yanagi and Takahashi, 1993]. The phase of the flow at these locations is opposite. These two regions correspond to areas where the surface elevation contours around amphidrous points meet the shore [Yanagi and Takahashi, 1993].

[13] The Shandong area of our studies is located north of the Yangtze River, about halfway up to the Shandong Peninsula. There the shore areas still have pronounced flood and ebb tides [Yanagi and Takahashi, 1993]. The flood tide component shows a structure that is indicative of a dividing



**Figure 4.** M2 surface elevation and phase structure, in cm/deg, simulated with a barotropic semidiurnal tidal model. The phase lines originate from the amphidromic points and are color coded according to elevation and angle. They are color coded as: 25/0 (blue) to 275/330 (red) by 25/30 (cm/deg). Elevation varies from 25 cm (blue) to 275 cm (red). Elevation increment is 25 cm and angle is  $30^\circ$ . The lines not connected to amphidromic points track only the elevation.

line between tidal ellipses that are cyclonic in the northern part of the Shandong region and anti-cyclonic in the southern part [Fang, 1994]. Along the shore the tidal magnitude variability of the area ranges from 1.2 m/s to 0.3 m/s [Valencia, 1987; Fang, 1994].

[14] The tidal motion across the topographic variations generates an internal tide and possibly higher frequency internal waves, which propagate away from the generation site [Baines, 1973, 1982]. These waves may steepen through nonlinear effects, after which frequency and amplitude dispersion sets in and the leading edge disintegrates into high-frequency solitary wave trains [Lamb, 1994; Brandt et al., 1997].

#### 2.4. Summer Hydrography

[15] For the Shandong area, hydrographic surveys are not available. As a result, the monthly averaged temperature and salinity distribution from the National Oceanographic Data Center (NODC) database was used.

[16] The west to east hydrographic structure at  $35^\circ\text{N}$  shows variability from the Chinese to the Korean coasts. Figure 5a displays some temperature change along the latitude section ( $121^\circ\text{E}$  to  $124^\circ\text{E}$ ). From the shallow areas along the Chinese coast to the middle of the Yellow Sea the thermocline deepens, from about 10 m to 25 m. Climatological 6-month averaged salinity distributions contain a 10-m mixed layer and exhibit an increase in salinity from longitude  $121^\circ\text{E}$  to  $124^\circ\text{E}$ .

[17] At the outskirts of the Shandong study area, in the vicinity of latitude  $35^\circ\text{N}$  and past longitude  $124^\circ\text{E}$ , summer surveys for the month of August are available. Lie [1986] has extracted temperature, salinity, and sigma-t distributions

from CTD casts made in August of 1983 and 1984, in the southeastern Hwanghae (Yellow Sea). These casts give us bounds on salinity, temperature, sigma-t, and the general structure at the outskirts of the area. From the NODC climatology and the surveys of Lie [1986], generic density structure functions are constructed that have the form of

$$\sigma_t = mz + A[1 - \tanh(z + b)], \quad (1)$$

where  $z$  is depth and  $m$ ,  $A$ , and  $b$  are arbitrary constants selected to match the density structure of the region for August.

[18] Figure 5b shows the background density fields that are used in the simulations. Stratifications with pycnoclines at depths of 10, 15, and 20 m are shown (upper 40 m only). For these stratifications, solitary waves will be waves of elevation/depression in the shallow/deep water, depending on the pycnocline location [Liu et al., 1998].

### 3. Generation and Propagation of Solitary Wave Trains

#### 3.1. Model

[19] The Lamb [1994] model is used for simulating the generation and propagation of solitary waves in the Yellow Sea. It consists of the Boussinesq equations with the Coriolis force in a two-dimensional cross-bank plane. The coordinates are defined with:  $x$  as across bank,  $y$  as along bank, and  $z$  as the depth.  $N$ , the Brunt-Väisälä frequency, is a function of depth and  $x$  (range). In the along-bank direction, the velocity is included but the derivatives are neglected (2.5-dimensional representation). The equations of the model are

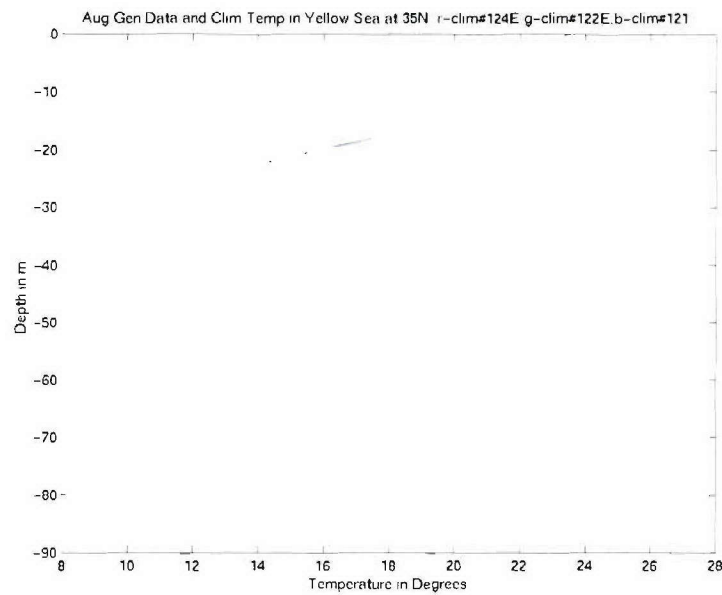
$$\mathbf{V}_t + (\mathbf{V} \cdot \nabla) \mathbf{V} - f \mathbf{V} \times \hat{\mathbf{k}} = -\nabla P - \hat{\mathbf{k}} \rho g, \quad (2)$$

$$\rho_t + \mathbf{V} \cdot \nabla \rho = 0, \quad (3)$$

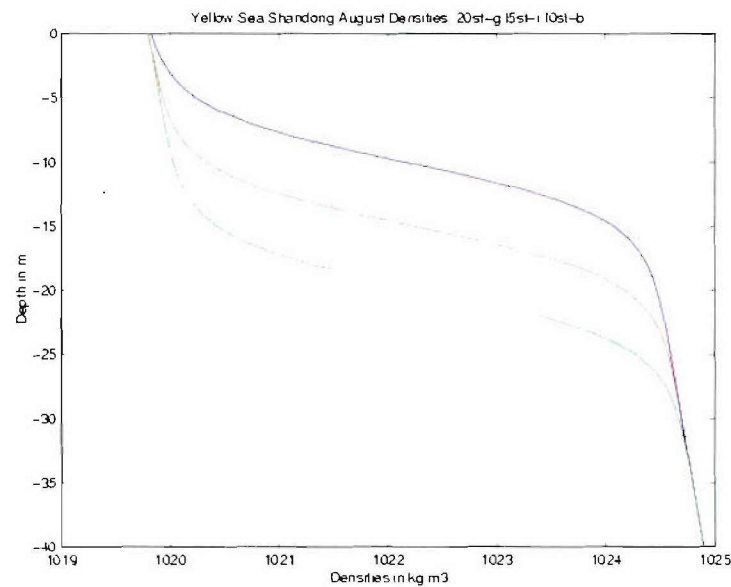
$$\nabla \cdot \mathbf{V} = 0, \quad (4)$$

where  $\mathbf{V}(u, v, w)$  is the velocity vector,  $\nabla$  is the three-dimensional vector gradient operator, subscript  $t$  denotes the time derivative,  $\rho$  is the density,  $P$  is the pressure,  $g$  is the gravitational acceleration,  $f$  is the Coriolis parameter taken as  $9 \times 10^{-5} \text{ s}^{-1}$  for a latitude of 40 degrees, and  $\hat{\mathbf{k}}$  is the unit vector along the  $z$  direction. In the three-dimensional equations (2)–(4) the partial derivatives with respect to  $y$  are neglected, i.e.,  $\frac{\partial}{\partial y}(\ ) = 0$ ; thus equations (2)–(4) are equivalent to equations (1a)–(1d) in Lamb's [1994] paper.

[20] Before the equations are solved, they are transformed to a terrain following coordinate system (sigma-coordinates) which leads to higher vertical resolution over the bank region. The equations are solved over a domain bounded below by the topography and a rigid lid above. The flow is forced by specifying a semidiurnal tidal inflow at the left boundary of the form  $V_T \sin(\omega t)$  where  $\omega$  is the  $M_2$  tidal frequency assumed to have a 12.4-hour period. The strength of the tidal current in the shallow water,  $V_T$ , varies between



(a)



(b)

**Figure 5.** (a) Temperature profiles from climatology at 35°N and 121°E blue line, 122°E green line, and 124°E red line. (b) Sigma-t densities with pycnoclines at depths of 10 m (blue line), 15 m (red line), and 20 m (green line).

0.3 and 1.2 m/s, typical of values in the Shandong region (see section 2.3). On the right boundary an outflow condition is used [Lamb, 1994]. The topographies used have already been discussed in section 2 (see Figure 2). The initial conditions are a state of rest with horizontally uniform density (section 2.4). The horizontal grid size is 20 m, for most cases, and the vertical sigma-coordinate

resolution consists of 60 grid points. The time step is tied to the Courant-Levi condition and varies from 1 s to 5 s.

### 3.2. Dynamics of Generation and Propagation

[21] The parameters for the different model runs are given in Table 1. We begin by considering Case 2 in detail. For Case 2, the thermocline depth is 15 m, the peak barotropic



**Table 1.** Simulation Parameters<sup>a</sup>

Case	$h_d$ , m	$H$ , m	$V_T$ , m/s	Topo	$d_H$ , km
1	15	70	1.2	a	150
2	15	70	0.7	a	240
3	15	70	0.7	a	300
4	15	70	0.35	a	240
5	10	70	0.7	a	240
6	10	40	0.7	a	240
7	10	40	0.7	b	200
8	20	70	0.7	a	240
9	20	70	1.2	a	240

<sup>a</sup>Here  $h_d$  is pycnocline depth,  $H$  is water depth,  $V_T$  is the tidal strength, Topo is the topography type ("a" being for cases with a finger, and "b" being for cases with the finger removed), and  $d_H$  is the length of the computational domain.

tidal velocity is 0.7 m/s, and the water depth is 70 m. Contour plots of the density field at various times are shown in Figures 6a–6e.

[22] Initially, the density field is horizontally homogeneous and there is no flow in the  $x$  direction. The prescribed semidiurnal tide, on the left boundary, accelerates the fluid in the off-bank direction. The presence of a ridge in the topography results in the generation of two initial depressions during the off-shelf flow. Each of these splits into two waves, each propagating in opposite directions. In Figure 6a the small depression over the ridge is a combination of two of these, and is predominantly comprised of the off-shelf depression formed over the first drop in the topography. The shoreward propagating depression formed over the first drop has steepened to form a hydraulic jump. Its shoreward propagation has been halted for a time by the supercritical tidal flow on the shelf. During on-shelf tidal flow the bottom of the depression is pushed up and a large jet of water rises well above the bottom. In the end, a wave of elevation is formed. One such wave is formed each tidal period as can be seen in Figure 6b, which shows the density field at 42 hours (about 3.4 tidal periods). Here the leading small depression at about 125 km is the off-shelf propagating depression formed to the lee of the ridge during the first tidal period. The first wave train to come off the shelf, at about 110 km, was formed from the off-shelf propagating depression formed over the first drop, between the shelf and the ridge, during the first tidal period. During the second period of off-shelf flow, it was just to the right of the ridge at the location where the second initial depression was formed in the first tidal period. Hence the creation of a depression to the lee of the ridge can only be seen during the first tidal period.

[23] After four tidal cycles a fourth solitary wave train is about to form from a large hydraulic jump at around 30 km (Figure 6c). The second solitary wave train, from the left, in Figure 6b has moved to 100 km (Figure 6c). Note that the spacing between the waves in the first packet has increased. This is the first train to come off the shelf and has evolved to a structure in which the individual waves in each packet get farther apart.

[24] Each tidal cycle generates wave propagating on the shelf and a wave packet propagating away from the shelf. This behavior is seen in other areas [Apel, 2003; Brandt et al., 1997; Warn-Varnas et al., 2003]. The waves of elevation on the shelf travel toward the shore and oscillate with the semidiurnal tidal motion. The amplitudes of the waves

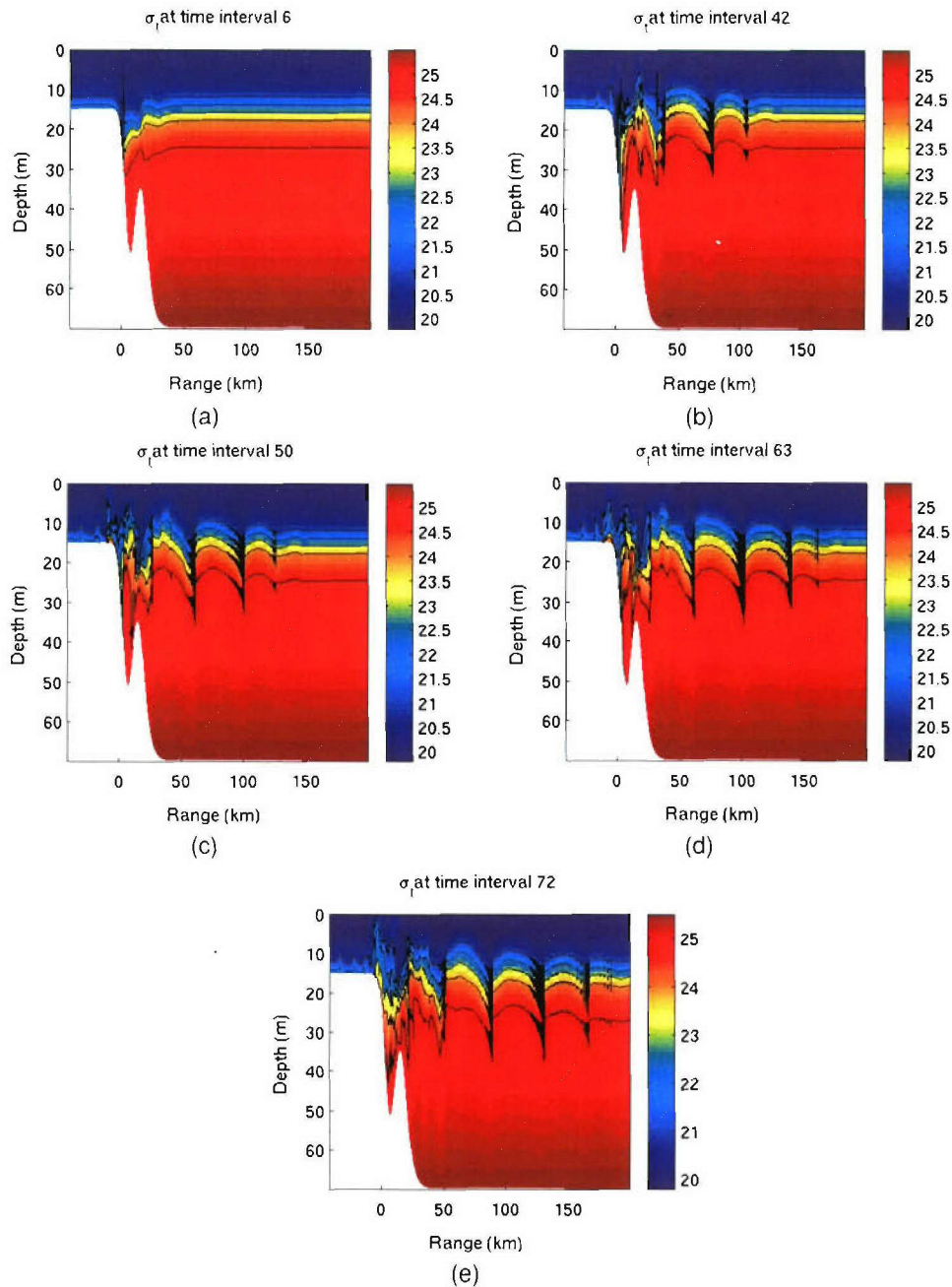
decrease through dynamical evolution, and they eventually disappear. At 63 hours or 5.1 semidiurnal tidal cycles into the simulation, there are four well-developed wave packets, with a fifth starting to form (Figure 6d). Note that the first three wave packets from the shelf show a dramatic increase in amplitude. This is largely due to the response over the shelf edge increasing in time, as discussed by Lamb [1994]. The third and fourth packets from the shelf are more similar in size (when compared at similar stages of their evolution). The individual waves in each packet grow in size for a while and then start to decay. They also get farther apart. This is particularly apparent in the first two packets away from the shelf shown in Figure 6e. The decrease in amplitude is a physical phenomenon. Numerical dissipation and boundary effects are minor influences.

[25] Note the recovery of the isopycnals toward the original equilibrium position before the next depressions of the new solitary wave train in the following tidal cycle. At the end of one tidal period, each isopycnal must have the same average height as it had at the start of the simulation. In the case of waves of depression propagating away from the generation site, conservation of mass implies that the isopycnals must lie above their initial height somewhere in the domain after a full tidal period (this is not true, for example, half a tidal period after the start of off-shelf flow). This occurs at the generation site where the dynamics cause the fluid to rebound and overshoot its initial height after being forced downward during off-shelf flow [Lamb, 1994]. The spacing between the wave trains tends to decrease toward the right boundary, indicating that the phase velocity decreases as the trains propagate to the far right. This is partly a consequence of the fact that the wave propagation speed is an increasing function of amplitude.

[26] The model simulations establish the generation of solitary waves in the shelfbreak area and the off-shelf propagation of solitary wave packets. The solitary waves are generated by semidiurnal tidal motion over topographic changes at the shelfbreak. SAR imagery also indicates solitary wave packets propagating off the shelf (sections 2.2 and 3.6), suggesting the generation of the wave packets at the shelfbreak. Solitary wave packet generation and propagation can occur in other areas of the Yellow Sea. Hsu et al. [2000] tracked solitary wave packets propagating from east to west. Most of these solitary wave packets indicate an origin southwest off the tip of Korea. Some of the solitary wave packets have an origin in the coastal area off China.

[27] The strength of the semidiurnal tide, together with the structure of topography, influences the size of the initial depressions formed over the bank edge during the off-bank flow. Lamb [1994] estimated the size of the initial pycnocline depressions that arise from variation in the prescribed tidal strength,  $V_T$ , and the topographic structure. He let the depression of volume  $V$  formed over the shelf slope have a characteristic length  $L$  and depth  $D$ . The length of the depression is determined by the width of the shelf or bank edge and an analysis of the volume displacement caused by the tide showed that the amplitude of the initial depression scales as  $D \sim V_T/L$ .

[28] The tidal parameter,  $V_T$ , was varied from 0.35 m/s to 1.2 m/s. These values reflect possible conditions in the Shandong area (see section 2.3). The consequences of

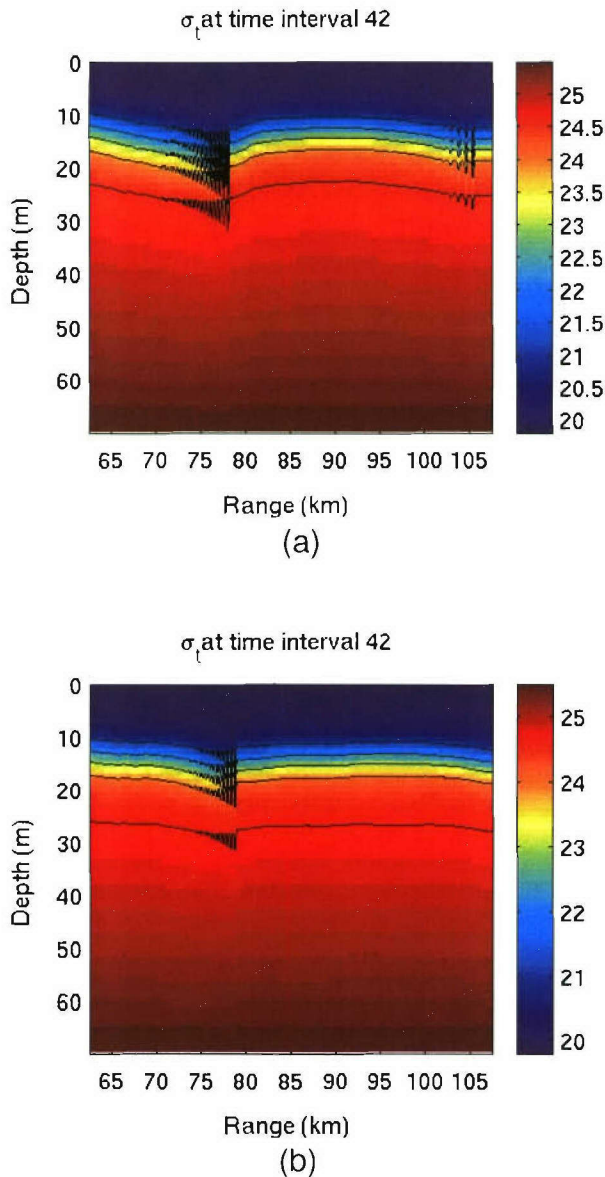


**Figure 6.** Model predicted evolution of solitary wave trains over semidiurnal tidal periods. Sigma-t density field for Case 2 in Table 1 at semidiurnal tidal periods of (a) 0.48, (b) 3.4, (c) 4.0, (d) 5.1, and (e) 6.1.

varying the tidal strength can be illustrated by comparing Cases 2 and 4 in Table 1. The only difference between the two cases is the strength of the tidal forcing which decreases from  $V_T = 0.7$  m/s for Case 2 to  $V_T = 0.35$  m/s in Case 4. A comparison of the results at 42 hours is shown in Figure 7. For a tidal forcing of  $V_T = 0.7$  m/s the first two wave trains to come off the shelf are located near 105 km and 78 km. The second wave train has a leading amplitude of about 7 m and a wavelength of 475 m (distance between wave crests) near the front of the train (Figure 7a). For a tidal forcing of  $V_T = 0.35$  m/s the previous first wave train to come off the shelf does not exist. The second solitary wave train has a

leading amplitude of around 4 m and a wavelength of 400 m at a distance of around 78 km (Figure 7b). As the tidal forcing increases, the volume of water displaced increases and results in larger initial depressions. As a result, the amplitudes and wavelengths of the initial solitary wave train that develops are larger. For the second solitary wave train, there is an increase in amplitude as the tidal forcing increases. The wavelength exhibits a small increase (from 400 m to 475 m) with increasing tidal forcing from 0.35 m/s to 0.7 m/s.

[29] For a thermocline located at 20 m, Cases 8 and 9 in Table 1, a corresponding analysis was conducted for tidal



**Figure 7.** Simulations at 3.22 semidiurnal tidal periods with tidal forcing of (a)  $V_T = 0.7$  m/s and (b)  $V_T = 0.35$  m/s.

forcings of 0.7 m/s and 1.2 m/s. The results, for the second wave train to come off the shelf at around 83 km, yield amplitudes of 8 m and wavelengths of 480 m for both tidal forcings. These are similar values to the previous case for a tidal forcing of 0.7 m/s. This suggests that once the tidal strength reaches a certain magnitude or saturation value (as for the cases of  $V_T = 0.7$  m/s and  $V_T = 1.2$  m/s), the amplitudes and wavelengths of the second solitary wave train (and higher) reaches a saturation limit also, and they tend not to increase further.

[30] Near the saturation value of amplitude and wavelength, the most pronounced effect of tidal forcing is on the first wave train that comes out. For a forcing of  $V_T = 0.35$  m/s, there is no first solitary wave train. For forcings of  $V_T = 0.7$  m/s and  $V_T = 1.2$  m/s the first wave train

increases in amplitude in relation to the tidal forcing magnitude.

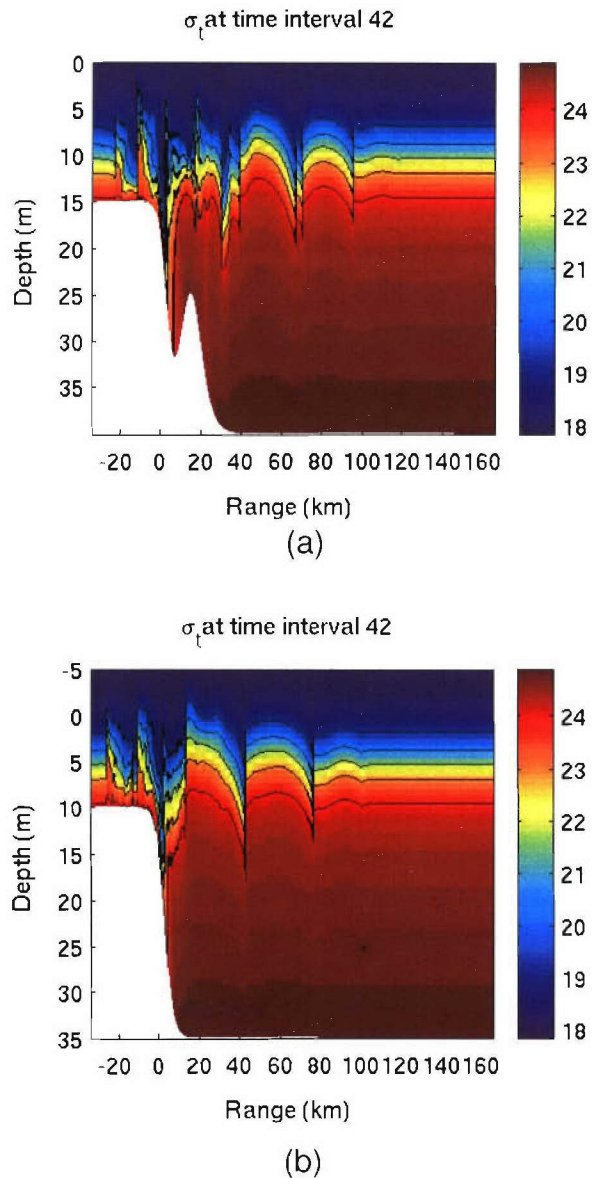
### 3.3. Effects of Topographic Variations

[31] The topographic structure in the Shandong area is described in section 2.1. Two transects across the shelf slope have been considered. Both consist of an initial drop, a rise, and then a second drop to their final depths of 40 and 70 m. Results from a simulation using a final depth of 40 m (Case 6 in Table 1) are shown in Figure 8a at 42 hours. This can be compared with Figure 6b, which shows results of Case 2 at the same time. Case 6 uses a thermocline depth of 10 m because a thermocline depth of 15 m did not result in the formation of a solitary wave train. The position of the first wave train to come off the shelf, for the 70 m depth, in Figure 6b is just past 100 km. For the 40-m-depth case the first wave train to come off the shelf is at about 95 km, suggesting a smaller phase speed. The next wave train has a double structure, with two solitary wave train structures close together at around 70 km (Figure 8a). The first jump (and solitary wave train to appear) evolved from the right propagating depression in the lee of the first drop reinforced by the left propagating depression from the second rise. Subsequently, for the following tidal cycles the modulation of the right propagating depression (from the first drop) by the left propagating depression from the second rise was such that a double structure solitary wave train resulted. In Case 2, with a deep water depth of 70 m, the two off-shelf propagating depressions were superimposed on each other, resulting in a single jump and wave train formed during each tidal period. A second double structured solitary wave train is starting to form at about 35 km. The wave trains that have evolved in the 40-m channel contain fewer waves and are much smaller than the trains in the 70-m channel shown in Figure 6b. On the other hand, on the shelf the internal bore structures are more pronounced in the 40-m channel simulations. This is due to the pycnocline being centered above the top of the shelf, resulting in more stratification in the shallow water in Case 6 than in Case 2.

[32] For the 40-m channel the effects of the second topographic rise (or finger) were investigated by removing it. All other aspects of the simulation were unchanged (Case 7).

[33] The results at hour 42 are shown in Figure 8b. The double structured wave trains have disappeared as expected. In Case 6 the first wave train is at 95 km at  $t = 42$  hours. This wave train is not present in Case 7, indicative of the fact that the left propagating depression from the second rise exerted a reinforcement effect.

[34] Along the SAR imagery and simulation track, there is a depth gradient from shallow to deep water, not only in the internal solitary wave propagation direction, but also in the along crest direction with the southern end of the train being over shallower waters than the northern end. As the internal solitary waves enter the shallow waters (depths of around 40 m) from the generation point, they disappear. The disappearance of internal solitary waves has been observed in regions where the waves shoal into a coastal area. In such situations, the pycnocline is at about mid-depth [Porter and Thompson, 1999; Porter et al., 2001]. This is not the case here, since the disappearance of internal waves is near the generation area. Our model simulations, however, indicate



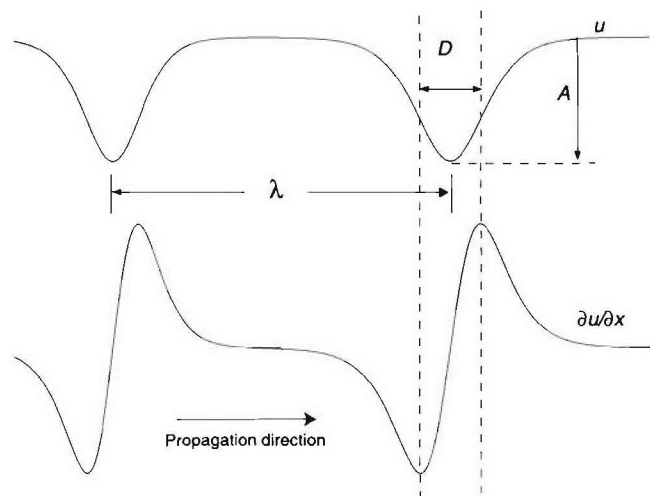
**Figure 8.** Simulations at 3.22 semidiurnal tidal periods with two topographies: (a) Case 6 in Table 1 and (b) Case 7 in Table 1.

that for a pycnocline depth of 20 m in a 40-m channel, internal solitary waves do not evolve as predicted by weakly nonlinear theory for symmetric stratifications [Liu *et al.*, 1998]. For other pycnocline depths in 40-m depth channels, such as 10 m, solitary waves do evolve. Such conditions are possible during some portion of the summer months.

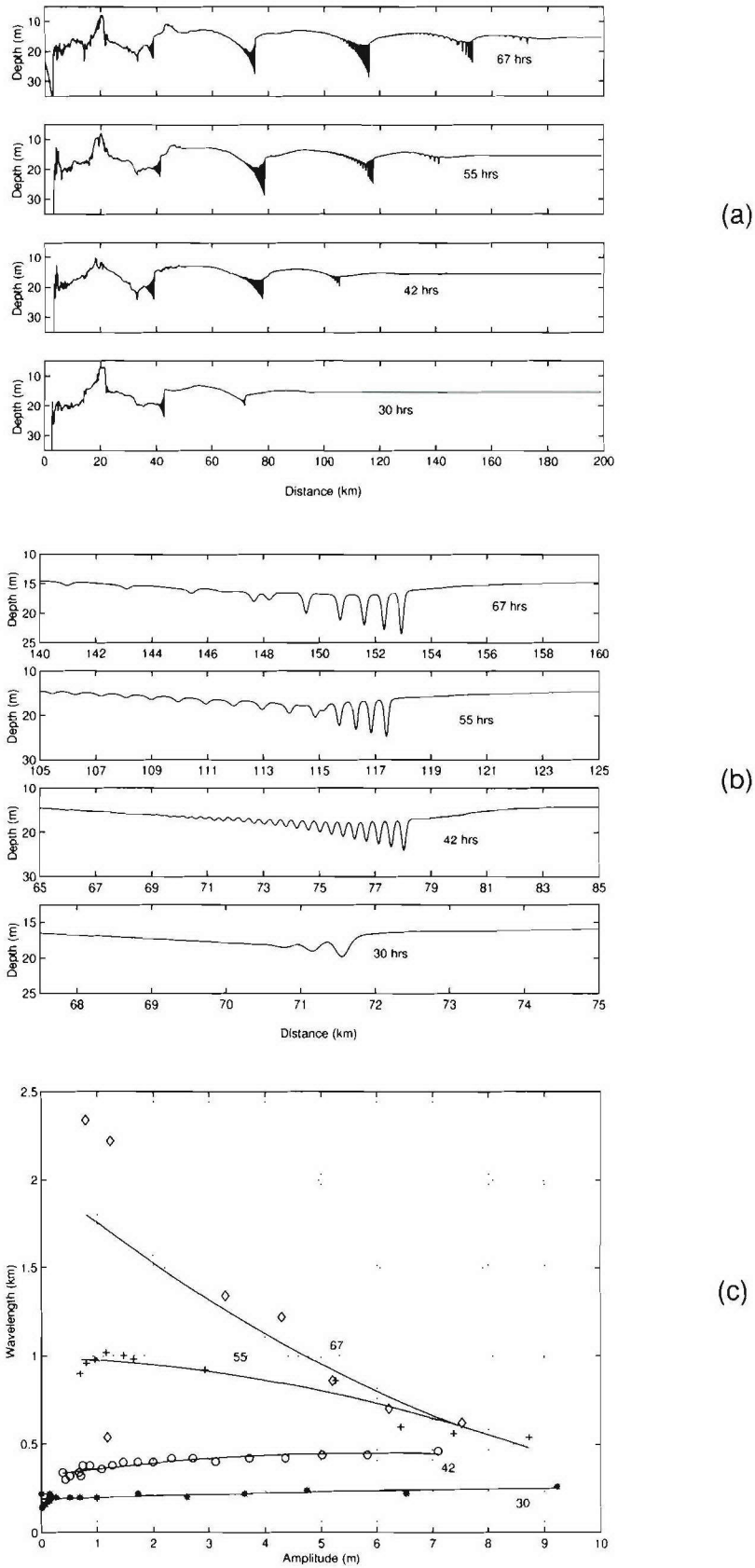
### 3.4. Dispersion Variations in the 70-m-Depth Channel

[35] The approach for the analysis of the wavelength and amplitude of individual wave trains is illustrated by the schematic diagram shown in Figure 9. Waves of depression have peak horizontal surface currents in the center of the wave in the direction of propagation. Thus peak surface convergence (max  $\partial u/\partial x$ ) occurs in the front half of the wave while peak surface divergence occurs in the second half of the wave. The distance between the extrema in  $\partial u/\partial x$

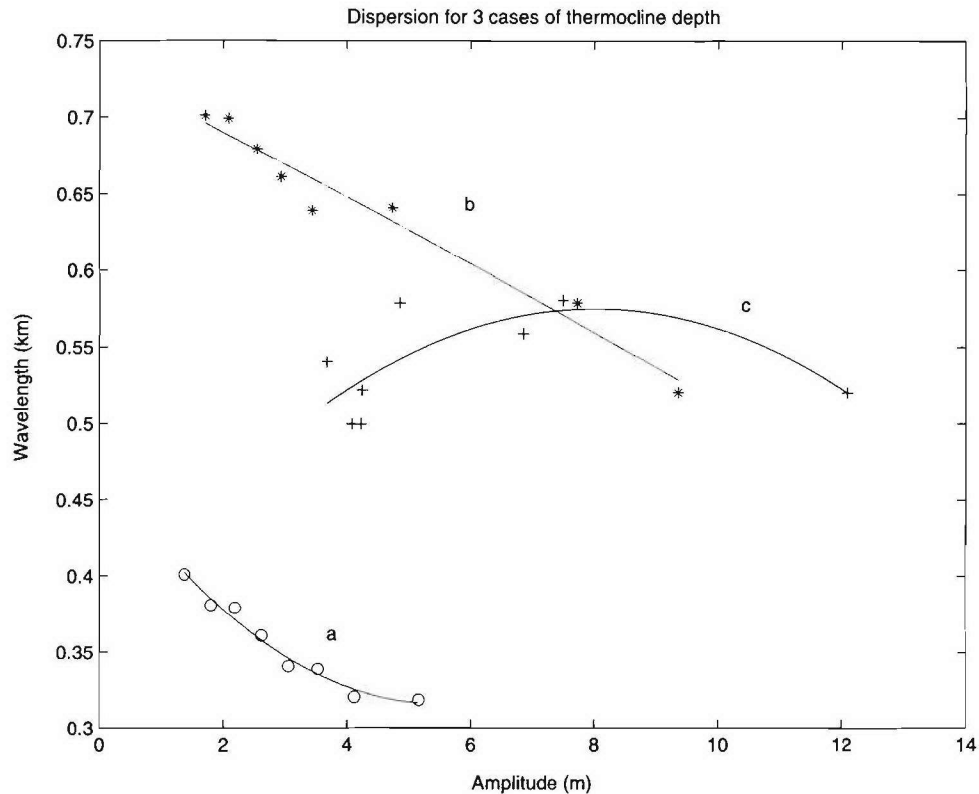
is called  $D$ . Regions of strong convergence and divergence can appear as bright and dark lines in SAR observations. The wavelength,  $\lambda$ , is defined as the distance between successive centers of troughs. The wavelength will be close to the distance between the convergences or bright lines in SAR observations. For well-separated solitary waves it is the distance between the waves, not a measure of the length of an individual wave. Except for very large times, the waves are not well separated in the model results. This definition of the wavelength is used in order to facilitate the interpretation of the Fourier spectra and the relation of the model simulations to SAR observations. Wave amplitudes are defined as the vertical displacement of an isopycnal from just ahead of an individual wave. An isopycnal in the middle of the thermocline is used, in this case with a value of  $\sigma_t = 22.5$ . This definition is somewhat problematic, particularly for the leading wave, as the wave train is in the depression of the internal tide and the internal tide changes shape with time. In particular, the isopycnal depressions rise, after the solitary wave packet, and then return to equilibrium (e.g., see Figure 6). The dispersive behavior of the second solitary wave train (to come off the shelf) for Case 2 in Table 1 has been analyzed at 30, 42, 55, and 67 hours. This is the case with a tidal forcing of  $V_T = 0.7$  m/s and a pycnocline depth of  $h_d = 15$  m depicted in Figure 6. Figure 10a shows the evolution of the solitary wave trains from 30 to 55 hours. At 42 hours the second train is located near 80 km. At 55 hours it has moved to near 120 km and has noticeably changed its structure. An enlargement of the second solitary wave train is displayed in Figure 10b. A distinct change in the structure of this train can be seen for the time interval of 42 to 55 hours. At 55 hours the back of the



**Figure 9.** Relationships of solitary waves to surface signatures. Arrow shows propagation direction. Upper curve is a typical isopycnal. Lower curve is  $\partial u/\partial x$  where  $u$  is the surface velocity (waves are propagating to the right). Positive/negative values are regions of surface convergence/divergence.  $D$  is the distance between the maxima in surface convergence/divergence which appear as bright and dark lines in SAR observations. The distance between waves,  $\lambda$ , will be referred to as the wavelength. In SAR images it is the distance between bright lines.



**Figure 10.** (a)  $\sigma_t = 22.5$  isopycnal at times of 30, 42, 55, and 67 hours, for Case 2 in Table 1. (b)  $\sigma_t = 22.5$  expanded view of isopycnals at times of 30, 42, 55, and 67 hours. (c) Amplitude-wavelength dispersion diagram for second solitary wave train, showing wavelength versus amplitude, for Case 2 in Table 1 at 30, 42, 55, and 67 hours. Solid lines are polynomial fits.



**Figure 11.** Dispersion diagrams at 50 hours exhibiting effects of pycnocline variations on second solitary wave train, showing wavelength versus amplitude, pycnocline at 10-m curve c, 15-m curve b, and 20-m curve a.

train has larger wavelengths than the front of the train. This trend is even more pronounced and dominant at 67 hours. The wavelengths as a function of amplitude distributions of the solitary wave train at the four times are shown in Figure 10c. At 30 hours the amplitudes vary from about 9.5 to 0.2 m and the wavelengths decrease from about 250 to 200 m. At 42 hours the amplitudes range is slightly less and the wavelengths have increased. They now vary from 425 at the front of the wave train to 350 m at the back. The large decrease in the amplitude of the leading wave is due to a drop in the size of the jump at the front of the wave. At 55 hours the structure of the second wave train changes, in the sense that the wavelengths tend to increase from the front to the back of the wave train with the amplitudes decreasing as before. To distinguish between different behaviors, a wave train with wavelengths decreasing from front to back will be called a type A configuration. Similarly, wave trains whose wavelengths increase from front to back will be called a type B configuration. The wavelength variation is from 550 to 1000 m. At 67 hours the amplitudes decrease, as before, and the wavelengths show more increase than at 55 hours from front to back, ranging from 625 to 2300 m. At the back of the wave train the distances between the centers of the depression increase appreciably as evidenced in Figure 6d.

[36] Away from the shelf and topographic changes, configuration B appears. When the configuration B occurs, the phase speeds of the depressions in the rear of the train decrease. Then the spaces between the depressions, in the rear, increase and the amplitude of the depressions

decreases. As the amplitude decreases, the wavelength increases.

[37] In the second wave train (to come off the shelf), the location of the center of the first depression was tracked in time. A straight line fit yields a propagation speed of 0.83 m/s. This is consistent with estimates from SAR observations (section 3.6), which yield values of 0.8 to 1.1 m/s. The model results were obtained with the summer stratification derived from climatology and available data (section 2.4). A thermocline depth of 15 m, Case 2 in Table 1, was found to yield the closest results to the SAR measurements (sections 3.6 and 3.7).

### 3.5. Effects of Pycnocline Variation

[38] The summer hydrography (section 2.4) was used to determine the density field used in the model simulations. The relevant parameter that describes the density structure for typical summer conditions is the pycnocline depth,  $h_d$ .

[39] For a tidal forcing of  $V_T = 0.7$  m/s, we considered the sensitivity of the model results to the stratification by comparing the results for the following thermocline depths: 10 m, 15 m, and 20 m (Cases 5, 2, and 8, respectively, in Table 1). The wavelength versus amplitude dispersion analysis of the second solitary wave train (to come off the shelf) at 50 hours is shown in Figure 11, for the three thermocline locations. For a 20-m location, Case 8 in Table 1, the amplitudes range from 5 m to 1.5 m and the wavelengths from 320 m to 400 m (curve “a” in Figure 11). The wavelengths increase from the front to the back of the

**Table 2.** Parameters of SAR Observations

	Bore 1	Bore 2	Packet 1	Packet 2	Packet 3	Packet 4	Packet 5
Distance, km	0	36 46	72 93	132	178	226	272
Phase speed $C$ , m/s		0.8 1.03	0.8 1.05	1.098	1.03	1.075	1.03
Dominant wavelength, m			630	930	1600	2300	

solitary wave train, indicating the presence of type B configuration. For a 15-m thermocline location, Case 2 in Table 1, the wavelengths increase from 530 m to 700 m and the amplitudes vary from 9.5 m to 1.5 m (curve “b” in Figure 11). The wavelength trend also exhibits a type B behavior. For a 10-m thermocline location, Case 5 in Table 1, the wavelength data exhibit scatter about the fitted curve that show wavelengths of around 525 m in front of the train, 510 m in the back, and 570 m in the middle, suggesting a transition between types A and B behavior. The amplitudes vary from 12 m to about 4.0 m (curve “c” in Figure 11). Overall, the largest wavelengths occur for Case 2, the 15-m thermocline, shown as curve “b” in Figure 11. This suggests a 15-m optimum thermocline location for maximum simulated solitary wave intensity. The phase speeds vary from 0.73 m/s to 0.82 m/s. The 15-m thermocline location yields a phase speed of 0.82 m/s, which is a lower bound in relation to SAR observations (Table 2).

### 3.6. Comparisons With SAR Observations and Discussion

[40] The SAR observations indicate a wave packet propagating away from shore along the track shown in Figure 1a. In the direction of the travel path, there is a depth gradient, from shallow to deep water, not only in the propagation direction but also in the along-crest direction with the southern end of the solitary wave train being over shallower water than the northern end. In addition, as the south end of the wave crest enters shallow waters, its signature tends to disappear (M. Teixeira, personal communication, 2002). The southern end of the signature is located around the 40-m depth region. Model simulations indicate that for a 15-m pycnocline in a water depth of 40 m, no solitary waves develop (section 3.3). As a result, we will only compare the 70-m channel simulations with the SAR data.

[41] Along the track there are the signatures of two internal hydraulic jumps and five solitary wave trains, shown in Figure 3a. A zoom of the first resolved solitary wave train is shown in Figure 3b, on a 20 km by 20 km grid. The distances between the bright lines represent the spacing between the train convergence locations (see Figure 9), and indicate the wavelength between the centers of the troughs associated with the depression of the isopycnals.

[42] A relationship between the half-width  $L$  of a solitary wave and the distance  $D$  between maximum points of surface convergence and divergence in a solitary wave can be derived. The derivation is based on the hyperbolic secant representation of a solitary wave [Small *et al.*, 1999] and gives the relationship

$$L = D/1.32. \quad (5)$$

We have estimated the distance  $D$  from the RADARSAT1 ScanSAR observations for the first wave train shown in

Figure 3b. Assuming a resolution of 100 m per pixel and measuring the first wavelength in the train, one obtains  $L = 75.7$  m (see Teixeira *et al.* [2005] for more details). The error is large, being  $\pm 37$  m (assuming an error of 50 m in the SAR image).

[43] The results of two-dimensional Fourier spectral analysis of the SAR images are summarized in Table 2, where the solitary wave trains are labeled from left to right. The listed wavelengths are for the most intense spectral peaks that occur for packets 1, 2, 3, and 4. For packet 5, there is not enough signal above background. The Fourier analysis reflects the wavelength around which most of the energy is concentrated. The set of wavelengths that we obtained for the solitary wave trains is 630 m, 930 m, 1600 m, and 2300 m (Table 2).

[44] The locations of the internal bores and solitary wave packets are listed in Table 2 relative to the first bright spot appearance or beginning. Bore 1 is located on the shelf-break. It is assumed that each solitary wave packet is generated at intervals of the semi-diurnal tidal period or 12.4 hours. With this assumption, the phase speeds are estimated along the track. They range from 0.8 to 1.098 m/s.

[45] For comparison with SAR, the simulation with a 15-m thermocline, Case 2 in Table 1, is used. This is the simulation whose second solitary wave train (that comes off the shelf) has the largest wavelengths at four tidal cycles (see Figure 11). The wave train is located at 100 km (Figure 6c). The calculated spectra are shown in Table 3. The dominant wavelength in the vicinity of 100 km is around 640 m and is practically at the 630-m value contained in the data (Tables 2 and 3). The agreement, however, changes as more and more solitary wave trains are generated and move through the 100 km location. Table 3 shows the calculated wavelengths at the various horizontal locations (labeled from left to right) for different trains that are generated during semidiurnal tidal cycles. The first train that propagates away from the shelf break region behaves differently from the other trains and represents a different dynamical state of evolution. Consider this to be the initial adjustment state.

**Table 3.** Model Results for Case 2 in Table 1 (240 km) for First Through Fifth Wave Trains<sup>a</sup>

	1	2	3	4	5
Tidal cycle	4	4	4		
Distance, km	65	100	130		
Wavelength, m	330	640	1300		
Tidal cycle	5.1	5.1	5.1	5.1	
Distance, km	60	100	140	165	
Wavelength, m	270	490	640	2700	
Tidal cycle	6.1	6.1	6.1	6.1	6.1
Distance, km	63	102	143	178	195
Wavelength, m	335	420	810	640/2300	3300

<sup>a</sup>The slash indicates another wavelength that is present. Distance is measured from the shelfbreak.

**Table 4.** Model Results for Case 3 in at Tidal Cycle 7.1 for First Through Sixth Wave Trains<sup>a</sup>

	1	2	3	4	5	6
Distance, km	95	138	179	211	224	.
Wavelength, m	340	640	1050/2100	550/2300	1300/2500	.

<sup>a</sup>The slash indicates another wavelength that is present. Distance is measured from the shelfbreak.

[46] The solitary wave trains propagate away from the shelf through the various horizontal locations or check points at which the spectra are calculated. Similar locations are chosen for comparing model predicted wavelengths with SAR measurements. At around 100 km the model predicted wavelength varies from 640 m to 420 m (disregarding the adjustment state) as the tidal cycle progresses from 4 to 6.1 (Figure 6e). The measurements (Table 2) show a 630-m wavelength at the location. In the vicinity of 130 km to 140 km the model results yield a variation of 640 m to 810 m while the data show 930 m. At around 170 km the modeled wave train is displaying an increased spacing between waves that is most pronounced toward the back of the wave packet. The resultant wavelength due to this increased spacing is around 2300 m (Table 3). The corresponding wavelength in the measurements is around 1600 m (Table 2). This is a situation where the model overpredicts the wavelength instead of underpredicting it. This suggests a change in the behavior of the measured solitary wave trains from type A to type B configuration that results in a sudden increase in wavelength size. The model results at ranges greater than 170 km also indicate such a possibility.

[47] The change in behavior of solitary wave trains is investigated further by considering a larger horizontal domain in which the solitary wave trains can propagate further relative to the previous simulation. Case 3, in Table 1. The horizontal domain is increased from 240 km to 300 km. The resolution is 60 grid points in the vertical, 12,000 grid points in the horizontal, for both cases. The depth of the ocean is 70 m for both cases. The horizontal grid spacing changes from 20 m to 25 m for the 300-km horizontal distance, Case 2 in Table 1.

[48] Table 4 shows the analyzed Fourier wavelengths for this case (Case 3 in Table 1). The simulations of Table 4 extend to 7.1 tidal cycles. The dominant large wavelengths show an abrupt increase from wave trains 1 and 2 to wave trains 3 and 4. This abrupt increase is also present in the data (Table 2). This reinforces the hypothesis of two behavior states, A and B.

[49] The variation of modeled wavelengths is due to several factors. As the solitary wave trains travel through the region, the isopycnals tend to return to an equilibrium position that becomes progressively higher than the original (Figure 6).

[50] Another source of discrepancy is the three dimensionality of the problem. The curvature effects in the 2.5-dimensional model that neglects the derivatives perpendicular to the 2-D plane are not represented, as well as any cross-plane dynamical processes that involve transport and exchange. The neglect of three-dimensional effects probably plays a role in the different characteristics of the solitary wave trains that propagate off the shelf break.

[51] Another parameter to consider is horizontal grid resolution. The results shown in Tables 3 and 4 were obtained with horizontal resolution of 20 m and 25 m, respectively. The 20- to 25-m horizontal resolutions resolve the internal solitary wave wavelengths that range from 630 m to 2300 m in the SAR observations (Table 2). The 20- to 25-m grid horizontal intervals are also within the 100-m pixel resolution of the SAR data and the half-width,  $L$ .

[52] The model simulations exhibit the presence of two behavior configurations, A and B, that have corresponding solitary wave train characteristics. These states of behavior are evolved by the dynamics of the model. SAR data and model simulation show an abrupt increase in wavelengths between some of the solitary wave trains. This suggests that the model formalism does contain dynamics similar to the ocean. The modeled wavelengths are within a factor of 2, or less, of wavelengths derived from SAR data. The simulated phase speeds range from 0.73 m/s to 0.83 m/s. The phase speeds estimated from the measurements range from 0.8 m/s to 1.1 m/s.

#### 4. Conclusion

[53] This work establishes the generation and propagation of solitary waves in the Shandong Peninsula region of the Yellow Sea. It is shown that generation and propagation of internal solitary waves occurs, over small topographic drops, along a southeastern track off the Chinese coast located south off the Shandong peninsula. SAR imagery indicates the presence of internal solitary waves along the same track and suggests their generation in the shallower shelf break region. Model results confirm the generation of internal solitary waves in the same off shelf area. On-shelf SAR imagery and model results show the presence of internal bores. The SAR observations are used for guiding and tuning the model simulations by comparing spectra of observed and modeled wavelengths. The tuned model yielded wavelengths that are within 2 or less of SAR data. Modeled wavelengths ranged from 335 m to 3300 m and amplitudes up to 9 m. Modeled phase speeds tended to be at the lower limit of phase speeds deduced from SAR data that ranged from 0.8 to 1.0 m/s. Both model simulations and SAR observations show the presence of two types of internal solitary wave structures configurations, A/B. This suggests that the model formalism does contain dynamics similar to the ocean. In configuration A, the wavelengths decrease toward the back of the packet. In configuration B, they increase toward the back of the packet. Configuration B tends to develop later in time. Mixtures of both configurations can occur in an internal solitary wave train.

[54] **Acknowledgments.** We gratefully acknowledge the many helpful suggestions made by the reviewers. This work was supported by the



Office of Naval Research under PE 62435N, with technical management provided by the Naval Research Laboratory.

## References

- Apel, J. R. (2003), A new analytical model for internal solitons in the ocean, *J. Phys. Oceanogr.*, 33(11), 2247–2269.
- Baines, P. (1973), The generation of internal tides by flat-bump topography, *Deep Sea Res. Oceanogr. Abstr.*, 20, 179–205.
- Baines, P. (1982), On internal tide generation models, *Deep Sea Res., Part A*, 29, 307–338.
- Brandt, P., A. Rubino, W. Alpers, and J. Backhaus (1997), Internal waves in the Strait of Messina studied by a numerical model and synthetic aperture radar images from the ERS 1/2 satellites, *J. Phys. Oceanogr.*, 27(5), 648–663.
- Chin-Bing, S. A., D. B. King, and J. E. Murphy (1993), Numerical simulations of lower-frequency acoustic propagation and backscatter from solitary internal waves in a shallow water environment, in *Ocean Reverberation*, edited by D. D. Ellis, J. R. Preston, and H. G. Urban, Springer, New York.
- Choi, B. H. (1999), *Digital Atlas for Neighboring Seas of Korean Peninsula* [CD-ROM], B. H. Choi, Kumho, Seoul (Available from bchoi@yurim.skku.ac.kr).
- Fang, G.-H. (1994), Tides and tidal currents in East China Sea, Huanghai Sea and Gohai Sea, in *Oceanology of China Seas*, vol. 1, edited by Zhou Di et al., pp. 101–112, Springer, New York.
- Hsu, M.-K., A. K. Liu, and C. Liu (2000), A study of internal waves in the China Seas and Yellow Sea using SAR, *Cont. Shelf Res.*, 20(4/5), 389–410.
- Hsu, M.-K., A. K. Liu, and L. M. Mitnik (2001), Study bottom topography in the Taiwan area with ERS SAR, paper presented at 11th Pacific Asian Marginal Seas/Japan East China Seas Study Workshop, Off. of Nav. Res., Cheju, Korea.
- King, D. B., S. A. Chin-Bing, and R. W. McGirr (1994), Effect of shallow water internal waves on broadband acoustic wave propagation, in *Environmental Acoustics: International Conference on Theoretical and Computational Acoustics*, vol. 2, edited by D. Lee and M. Shultz, pp. 793–808, World Sci., Hackensack, N. J.
- Lamb, K. (1994), Numerical experiments of internal wave generation by strong tidal flow across a finite amplitude bank edge, *J. Geophys. Res.*, 99(C1), 848–864.
- Lie, H.-J. (1986), Summertime hydrographic features in the southeastern Hwanghae, *Prog. Oceanogr.*, 17, 229–242.
- Liu, A. K., Y. S. Chang, M.-K. Hsu, and N. K. Liang (1998), Evolution of nonlinear internal waves in the East and South China Seas, *J. Geophys. Res.*, 103(C4), 7995–8008.
- Naimie, C. E., C. A. Blain, and D. R. Lynch (2001), Seasonal mean circulation in the Yellow Sea: A model-generated climatology, *Cont. Shelf Res.*, 21(6/7), 667–695.
- Porter, D. L., and D. R. Thompson (1999), Continental shelf parameters inferred from SAR internal wave observations, *J. Atmos. Oceanic Technol.*, 16, 475–487.
- Porter, D. L., D. R. Thompson, W. Alpers, and R. Romeiser (2001), Remotely sensed ocean observations of the Coastal Mixing and Optics site from synthetic aperture radars and advanced very high resolution radiometers, *J. Geophys. Res.*, 106(C5), 9623–9638.
- Small, J., Z. Hallock, G. Pavey, and J. Scott (1999), Observations of large amplitude internal waves at the Malin Shelf edge during SESAME 1995, *Cont. Shelf Res.*, 19(11), 1389–1436.
- Teixeira, M., A. C. Warn-Varnas, J. Apel, and J. Hawkins (2005), Analytical and observational studies of internal solitary waves in the Yellow Sea, *J. Coastal Res.*, in press.
- Valencia, M. (1987), Summary report, in *International Conference on the Yellow Sea, Occas. Pap.* 3, pp. 88–90, East-West Environ. and Policy Inst., Honolulu, Hawaii, 23–27 June.
- Warn-Varnas, A., S. A. Chin-Bing, D. B. King, Z. Hallock, and J. Hawkins (2003), Ocean-acoustic solitary wave studies and predictions, *Surv. Geophys.*, 24, 39–79.
- Weston, D. E. (1992), Mechanisms of ocean acoustic attenuation: Scattering by internal solitons, by sea surface waves, and by fish, *J. Acoust. Soc. Am.*, 92, 3435–3437.
- Yanagi, T., and S. Takahashi (1993), Seasonal variation of circulation in the East China Sea and the Yellow Sea, *J. Oceanogr.*, 49, 503–520.
- Zhou, J. X., X. Z. Zhang, and P. H. Rogers (1991), Resonant interaction of sound wave with internal solitons in coastal zone, *J. Acoust. Soc. Am.*, 90, 2042–2054.

S. A. Chin-Bing, D. B. King, and A. C. Warn-Varnas, Naval Research Laboratory, Stennis Space Center, MS 39529, USA. (varnas@nrlssc.navy.mil)

J. A. Hawkins, Planning Systems Inc., Slidell, LA 70458, USA.

K. G. Lamb, University of Waterloo, Waterloo, Ontario, N2L 3G1 Canada.

M. Teixeira, Polytechnic University of Puerto Rico, Hato Rey, 00919 Puerto Rico.